IIETA International Information and Engineering Technology Association
Advancing the World of Information and Engineering

Traitement du Signal
Vol. 40, No. 3, June, 2023, pp. 1045-1054
Journal homepage: http://iieta.org/journals/ts

Advanced COVID-19 CT Image Segmentation Using a Hybrid Undecimated Wavelet Transform, Fuzzy Clustering, and Anisotropic Diffusion Approach

Messaouda Larbi[1], Hilal Naimi[2*], Mohammed Bourennane[2]

[1] Faculty of Science and Technology, University of Djelfa, Djelfa 17000, Algeria
[2] Laboratoire de Modélisation Simulation et Optimisation des Systèmes Complexes Réels, University of Djelfa, Djelfa 17000, Algeria

Corresponding Author Email: naimihilal87@gmail.com

https://doi.org/10.18280/ts.400320

Received: 24 January 2023
Accepted: 6 March 2023

Keywords:
undecimated wavelet transform, fuzzy C-means clustering, anisotropic diffusion, COVID-19

ABSTRACT

Early detection of Coronavirus Disease 2019 (COVID-19), an infectious disease caused by the SARS-CoV-2 virus, is crucial in minimizing the risk of mortality and limiting its spread, particularly among asymptomatic individuals. Computed tomography (CT) scans of the chest are commonly employed for diagnosing this condition, necessitating the development of segmentation techniques for analyzing these images effectively. However, segmenting COVID-19 CT images poses considerable challenges due to the indistinct boundaries between gray and white matter, as well as the homogeneous and ambiguous structures within the regions. To address these issues, we propose a hybrid approach that combines Undecimated Wavelet Transform (UWT), Fuzzy Clustering (FC), and Anisotropic Diffusion Filter (ADF). Our method involves utilizing UWT to denoise CT images in the frequency domain, followed by an advanced fuzzy clustering technique based on texture features and local gray value entropy for autonomous segmentation of CT images. The segmented images are then processed with ADF to eliminate uncertainty and noise. The performance of our proposed method was evaluated visually and through similarity measurements using an open-source dataset. A comparative analysis with alternative segmentation methods was conducted using multiple metrics, including Dice, Jaccard, Precision, Accuracy, Sensitivity, F-measure, MCC, and Specificity. Our results demonstrate that the proposed hybrid approach significantly enhances the detection of COVID-19 from CT images.

1. INTRODUCTION

COVID-19, a lethal pandemic caused by the novel coronavirus, has had a profound global impact [1-3]. The Reverse Transcription Polymerase Chain Reaction (RT-PCR) remains a primary diagnostic method for detecting, tracking, and studying the virus. However, it necessitates time-consuming procedures in highly controlled environments, with test results typically taking up to four hours [2]. Furthermore, the potential for false-negative RT-PCR results pose a significant public health risk. Medical radiology imaging has emerged as an ultra-rapid alternative for detecting suspected or asymptomatic cases of COVID-19, which can rapidly progress to viral pneumonia and manifest as severe lung disease. Studies have demonstrated that computed tomography (CT) scans are more sensitive than RT-PCR tests for detecting the infection [3]. Consequently, accurately identifying the region of infection can reduce the time radiologists spend analyzing test results.

Segmentation of CT images is considered one of the most challenging processes due to the presence of heterogeneous elements, textures, and edges [4]. As a result, developing effective pattern recognition and computer vision solutions for CT images has proven difficult [5]. Various researchers have proposed diverse segmentation algorithms for CT images, primarily focusing on the gray value distribution of pixels within chest images depicting gray matter, white matter, and pneumonia infections [6]. Consequently, segmentation techniques can be broadly classified as clustering, fuzzy, or thresholding-based methods.

Clustering algorithms have been widely used for medical image classification [7], with similarity and dissimilarity serving as the primary criteria for segmenting grayscale values. Clustering approaches can be divided into soft and hard clustering methods [8]. Fuzzy clustering (FC) is a soft clustering algorithm that assigns each pixel's gray value to a distinct cluster based on distance measurements [9].

Numerous thresholding techniques, such as Watershed [10], automatic selection [11], Otsu's global [12], adaptive [13], and iterative [14], have been employed for CT image segmentation. Recently, wavelet transform (WT) methods have gained popularity for medical image segmentation tasks [15]. Mohsen et al. [16] utilized principal component analysis, discrete wavelet transforms, and deep learning to detect tumors; however, their evaluations were limited to MRI brain image data.

While deep learning approaches have demonstrated remarkable performance in image segmentation, they require extensive training with numerous images [17], presenting a challenge for applications with limited image resources. In this context, unsupervised methods, such as clustering, are preferable, as they do not require additional images for training.

Despite the numerous CT image segmentation techniques developed by image analysts and researchers, most are tailored to specific conditions. For instance, expert and belief systems require accurate visualization of CT images for making correct inferences in information fusion. Moreover, there is an urgent need for a method that is not only effective for various CT images but also expeditious enough to support clinicians in saving time and lives.

In light of the aforementioned literature, we propose a CT image segmentation approach that combines undecimated wavelet fuzzy clustering and an anisotropic diffusion filter (ADF) to address the uncertainty, noise, low resolution, and imprecision in COVID-19 CT images. This work is motivated by the desire to improve the segmentation of CT images depicting COVID-19 infections and help limit disease progression.

The main contributions of this work include:

- Proposing an image segmentation model for COVID-19 CT images using a hybrid approach combining Undecimated Wavelet Fuzzy Clustering and Anisotropic Diffusion for segmenting chest CT images of COVID-19 infected individuals.
- Testing the proposed model with a collection of COVID-19 CT images sourced from various datasets.
- Evaluating the performance of our model by comparing it with previous works using multiple performance metrics, including Dice, Jaccard, Precision, Accuracy, Sensitivity, F-measure, MCC, and Specificity.

2. PREREQUISITES FOR THE SUGGESTED METHOD

A hybrid Method for precisely segmenting CT images of COVID-19 was suggested. The method was created primarily to remove abnormalities, like blind noise from CT scans. In order to conserve energy, the initial step of the proposed technique was to remove noise by employing UWT. The resulting image is then improved for better vision. The image was then segmented using FCMC, and an ADF was utilized to detect COVID-19 more effectively. In this part, a full description of the suggested method is presented. Figure1 depicts a block diagram of the suggested method for the automatic segmentation of CT images.

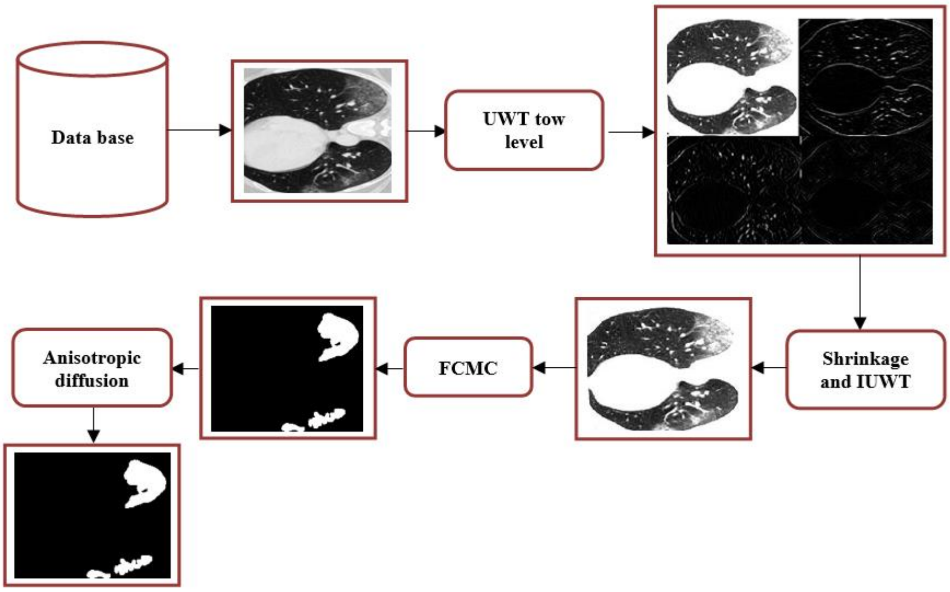

Figure 1. Block diagram of the approach that was proposed

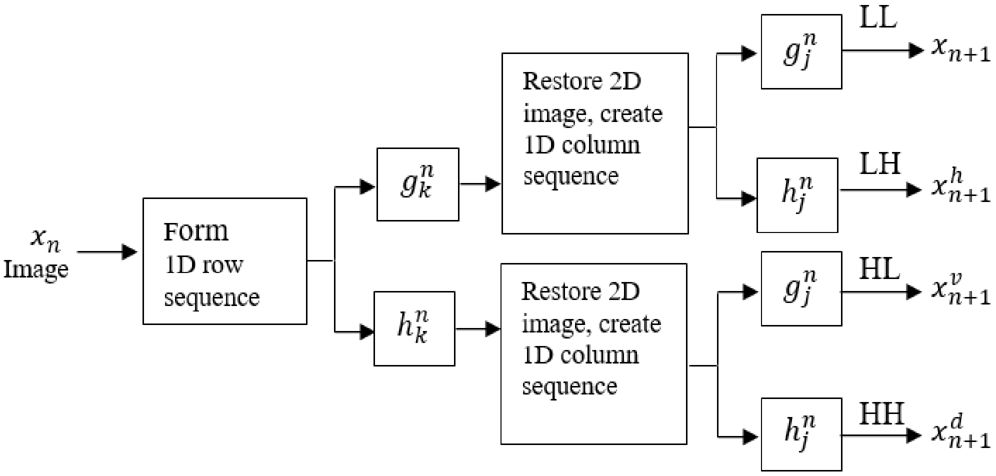

Figure 2. One level analysis filter bank for 2D UWT

2.1 Undecimated wavelet

Nason and Silverman [18] suggested the undecimated wavelet transform (UWT) to tackle the shift invariance and nonredundancy difficulties in the discrete wavelet transform [19, 20]. The initial signal is not decimated by UWT. Instead of down sampling the signal after applying low pass or high pass filters, it modifies the filters at each level by padding with zeros [21]. When compared to classical wavelets, the UWT sub signals from the analysis have the same size as the original signal. UWT is an excellent choice for our method because it provides for more precise understanding of the detail coefficients and corresponding approximation. UWT exhibited low-cost computing as well [22, 23]. As a result, we used UWT to resolve the energy consumption time series data, generate identifiable high frequency and low frequency components known as details and approximation, and then supply these components into the transformer.

The undecimated wavelet transform approximation sub-band depicts the time-series' overall trend, whilst the detail sub band reflects small series differences. The UWT separates high and low frequencies by breaking down the time series with a combination hierarchical of high pass and low pass wavelet filters. Figure 2 depicts the implementation of an analysis filter bank for a one level 2D UWT. This structure generates three detailed sub-images (HL, HL, HH) that correspond to three different directional orientations (Horizontal, Vertical, and Diagonal), as well as a lower resolution sub-image LL. On the LL channel, the filter bank structure can be iterated similarly to produce multi-level decomposition.

Consider x to be an image of size N^{x}M. UWT level n decomposition equation is [24]:

$$\begin{cases} x_{n+1}(a,b) = \sum_j \sum_k g_j^n g_k^n x_n(a+j, b+k) \\ x_{n+1}^h(a,b) = \sum_j \sum_k h_j^n g_k^n x_n(a+j, b+k) \\ x_{n+1}^v(a,b) = \sum_j \sum_k g_j^n h_k^n x_n(a+j, b+k) \\ x_{n+1}^d(a,b) = \sum_j \sum_k h_j^n h_k^n x_n(a+j, b+k) \end{cases} \tag{1}$$

where, a=1,2,…,N and b=1,2,…,M, g_j^n and g_k^n are low pass filters, h_j^n and h_k^n are high pass filters, x_n and x_{n+1} respectively represent the low frequency sub-band at levels n and n+1. While, x_{n+1}^h, x_{n+1}^v and x_{n+1}^d are represent the horizontal, vertical and diagonal detail coefficients, respectively, at level n+1.

The IUWT formula may be calculated as follows [24]:

$$\begin{aligned} \tilde{x}_n(a,b) = & \sum_j \sum_k \tilde{g}_j^n \tilde{g}_k^n \tilde{x}_{n+1}(a+j, b+k) \\ & + \sum_j \sum_k \tilde{h}_j^n \tilde{g}_k^n \tilde{x}_{n+1}^h(a+j, b+k) \\ & + \sum_j \sum_k \tilde{g}_j^n \tilde{h}_k^n \tilde{x}_{n+1}^v(a+j, b+k) \\ & + \sum_j \sum_k \tilde{h}_j^n \tilde{h}_k^n \tilde{x}_{n+1}^d(a+j, b+k) \end{aligned} \tag{2}$$

With $\tilde{g}_j^n$ and $\tilde{g}_k^n$ represent the reconstruction of low pass filters, $\tilde{h}_j^n$ and $\tilde{h}_k^n$ represent the reconstruction of high pass filters, $\tilde{x}_n$ and $\tilde{x}_{n+1}$ respectively represent the reconstruction low frequency sub-band at levels n and n+1. $\tilde{x}_{n+1}^h, \tilde{x}_{n+1}^v$ and $\tilde{x}_{n+1}^d$ represent the reconstructed horizontal, vertical and diagonal detail coefficients, respectively.

Applying a one dimensional undecimated wavelet transform to columns and rows of an image, followed by shrinkage (threshold) denoising of a signal of one dimensional, is the essence of image threshold denoising. When the wavelet coefficients' absolute value exceeds a particular shrinkage, the soft shrinkage function is equal to minus the shrinkage; otherwise, it is equal to 0. This is referred to as [20, 25]:

$$\begin{cases} z = soft(\omega) = sgn(\omega)\max\left(|\omega| - \lambda, 0\right), |\omega| > \lambda \\ z = soft(\omega) = 0, |\omega| \le \lambda \end{cases} \tag{3}$$

With ω and z respectively represent the input and output wavelet coefficients, σ the noise level might be known or unknown.

λ is the selected Shrinkage value defined as:

$$\lambda = \sigma\sqrt{2\log\left(N\right)}$$

where, N is the signal's size.

2.2 Fuzzy C-means clustering

To obtain segmented results, Fuzzy C-Means Clustering was used. The segmented images were then passed around an ADF to eliminate image-based uncertainties, yielding the eventual segmented area.

In this research, CT images are been segmented using unsupervised Fuzzy C-Means. FCMC was carefully chosen because it is regarded as one of the most effective pixel-based methods [26]. FCM includes an iterative process in which the dissimilarity measure, in the form of Euclidean distance, is minimized by upgrading the cluster centers and membership values in accordance with the following formulas [27]:

$$\mu_{tj} = \frac{1}{\sum_{k=1}^{C} \left(\frac{d_{tj}}{d_{tk}} \right)^{\frac{2}{m-1}}} \tag{4}$$

$$v_j = \frac{\left(\sum_{i=1}^{N} \left(\mu_{ij}\right)^m x_i \right)}{\left(\sum_{i=1}^{N} \left(\mu_{ij}\right)^m \right)}, \forall j = 1, 2, \ldots\ldots\ldots C \tag{5}$$

The principal aim is to find the minimum value of the objective function:

$$J\left(U,V\right) = \sum_{i=1}^{N} \sum_{j=1}^{C} \left(\mu_{ij}\right)^m \left\| x_i - v_{ij} \right\|^2 \tag{6}$$

This iterative procedure is repeated until a user-defined termination criterion is met.

2.3 Anisotropic diffusion filter

Anisotropic diffusion (AD) and isotropic diffusion (ID) are the two diffusion techniques used in image filtering. ADF outperforms IDF as an image filtering technique, in terms of preserving image detail [28]. Both diffusion methods utilize the averaging operation. Because IDF executes the averaging process over edge and corner areas, which obscures important information and disturbs the fine details, the averaging method distorts image information [29]. However, despite the fact that ADF uses the averaging operation here as well, it only does so on either side of an object, edge, or boundary, giving it an advantage over IDF. It does not obscure essential details, but rather smoothest the best data point by computing the gradient for supplied image space [28, 30], and this procedure is referred to as the "edge pausing function". The form of it is as follows:

$$\frac{\partial I(x,y,t)}{\partial t} = div\left(g\left(\left\|\nabla I(x,y,t)\right\|\right)\nabla I(x,y,t)\right) \quad (7)$$

With t represents the time parameter, I(x, y, 0) is the original image, I(x, y, t) denotes the gradient of the image I(x, y) at time t, and (·) represents the conductance model.

The conductance (·) is chosen so that the diffusion retains a null impact at the boundaries (*h*→∞) and produces its highest value inside homogeneous zones (*h*→0). Following is a model for this formulation:

$$\lim_{h\to 0} g(h)=1, \qquad \lim_{h\to\infty} g(h)=0,$$

To put it another way, relatively small intensity gradient values may be able to obstruct conduction in the case when the value of the conductance function is less. In the latter scenario when the conduction function value is greater, it refuses the output values of contingent intensity gradients. The following equations represent the most used conductance functions:

$$g_1(h) = \exp\left(-\left(\frac{h}{k}\right)^2\right) \quad (8)$$

$$g_2(h) = \frac{1}{1+\left(\frac{h}{k}\right)^2} \quad (9)$$

With "k" stands for the value of the "gradient magnitude threshold parameter," charge of administering diffusion speed or velocity. Eq. (8) offers a suitable and relevant solution for dealing with issues with high edge contrast problem statements. In contrast, Eq. (9) is better suited to a larger range of problem statements.

3. MATERIALS

3.1 Dataset acquisition for CT

In hospitals, COVID-19 pneumonia is typically diagnosed using a chest x-ray [31]. Because CT has better visibility than a chest x-ray, consequently, this research will focus on CT for its experimental investigation.

This research examined the COVID-19 pneumonia image CT database [31] to test the performance of the proposed image segmentation method. This database is made up of 100 CT and has a resolution of 512×512 pixels; additionally, all of the images that are currently available are linked to Ground-Truth-Images (GTI).

3.2 Quality metrics

In this study, a variety of metrics, including Dice, Jaccard, Precision, Accuracy, Sensitivity, Fmeasure, MCC, and Spectivity, are used to measure the correct and/or incorrect segmentation of COVID-19 that is detected in CT images. This is done in order to evaluate the performance of the effectiveness of our technique with various techniques. In this section, we will discuss the evaluation metrics that were used in this study.

The abbreviations for "True Positive", "True Negative" and "False Positive" are "TP","TN" and "FP" respectively.

3.2.1 Dice criterion

The Dice criterion [32] is a method that can be used to measure the accuracy of segmentation, and it is computed using the following formula:

$$Dice = \frac{2\left|S_g^1 \cap S_t^1\right|}{\left|S_g^1\right| + \left|S_t^1\right|} = \frac{2TP}{2TP+FP+FN} \quad (10)$$

3.2.2 Jaccard

The Jaccard index (JAC) [32] is determined as the intersection among two sets divided by the union of both sets. This can be written as follows:

$$JAC = \frac{\left|S_g^1 \cap S_t^1\right|}{\left|S_g^1 \cup S_t^1\right|} = \frac{TP}{TP+FP+FN} \quad (11)$$

The Jaccard score has a value range of 0 to 1. When the Jaccard score is higher, the image segmentation comes out looking better.

Mention that the Jaccard score is the most essential metric to evaluate the segmentation result performance in many of the works that have been published on the subject of medical image segmentation [32].

3.2.3 Accuracy

Determines how effectively a binary segmentation technique can recognize or rule out a condition [33]:

$$accuracy = \frac{TP+TN}{FP+FN+TP+TN} \quad (12)$$

3.2.4 Precision

In actuality, the precision, also known as the Positive Predictive Rate (PPR), is the ratio of the accurate statistical results to those of the diagnostic tests, or, to put it another way, the real positive results:

$$\Pr ecision = \frac{TP}{TP+FP} \quad (13)$$

3.2.5 Sensitivity

The sensitivity rate, also known as the true positive rate, indicates the proportion of lesions that are found:

$$sensitivity = \frac{TP}{TP+FN} \quad (14)$$

3.2.6 F-measure

The F-measure [34] is a metric that is used quite frequently to evaluate segmentation results. It is composed of the harmonic average of the performance measures for precision (13) and sensitivity (14), which are as follows:

$$F = \frac{2TP}{2TP + FN + FP} \quad (15)$$

3.2.7 Matthews correlation coefficient

In point of fact, the Matthews correlation coefficient (MCC) is a measurement that determines the correlation between both predicted and labels of ground truth [34].

The MCC values can range from -1 to 1, with a value of -1 indicating a completely disjoint prediction and a value of 1 indicating an ideal prediction.

$$MCC = \frac{TN.TP - FN.FP}{\sqrt{(TN+FP).(TN+FN)(TP+FP).(TP+FN)}} \quad (16)$$

3.2.8 Specitivity

The term True Negative Rate (TNR) actually indicates the capacity of the segmentation technique to eliminate redundant regions or regions wherein plaques are not present:

$$specificity = \frac{TN}{TN + FP} \quad (17)$$

4. EXPERIMENTAL RESULTS

This section presents the experimental results that were obtained by contrasting the quantitative and visual effectiveness of the proposed approach to detection COVID-19 against the other current techniques that have been satisfactorily applied to a variety of domains with good performance, including Inf-Net [35], U-Net [36], and U-Net++ [37]. In order to accomplish this object, the simulation experiment was conducted out on seven different medical images taken from database [31].

Quantitative Results: Statistical analysis was conducted applying eight metrics: Dice, Jaccard, Precision, Accuracy, Sensitivity, Fmeasure, MCC, and Specitivity. The quantitative outcomes are presented in Table 1. The values that were achieved using the proposed approach were highlighted in bold if they were superior to the values that were obtained through the other methods. When the values for Dice, Jaccard, Precision, Accuracy, Sensitivity, Fmeasure, MCC, and Spectivity are high, the larger the quantity of contrast information conveyed from the input images to the resultant segmented images. The proposed approach performs significantly better than Inf-Net, U-Net, and U-Net++ in terms of Dice, Jaccard, Precision, Accuracy, Sensitivity, Fmeasure, MCC, and Specitivity. In Table 1, the remaining seven COVID-19 images provided additional evidence that the proposed strategy is effective. Again, the findings demonstrated that the proposed method is effective in determining whether or not a patient has a lung infection based on different images. The proposed model is intended to serve as a diagnostic assistant, and it is anticipated that it will provide more information regarding the affected regions. In addition, we measure the amount of time it takes the proposed approach to run in comparison to the other techniques. The length of time each image is displayed for can be found in Table 1. Particularly in comparison to Inf-Net, U-Net, and U-Net++, the proposed approach is noticeably quicker. In a comprehensive analysis, we can observe that the proposed approach performs the very best when compared to other techniques in both quantitative evaluations.

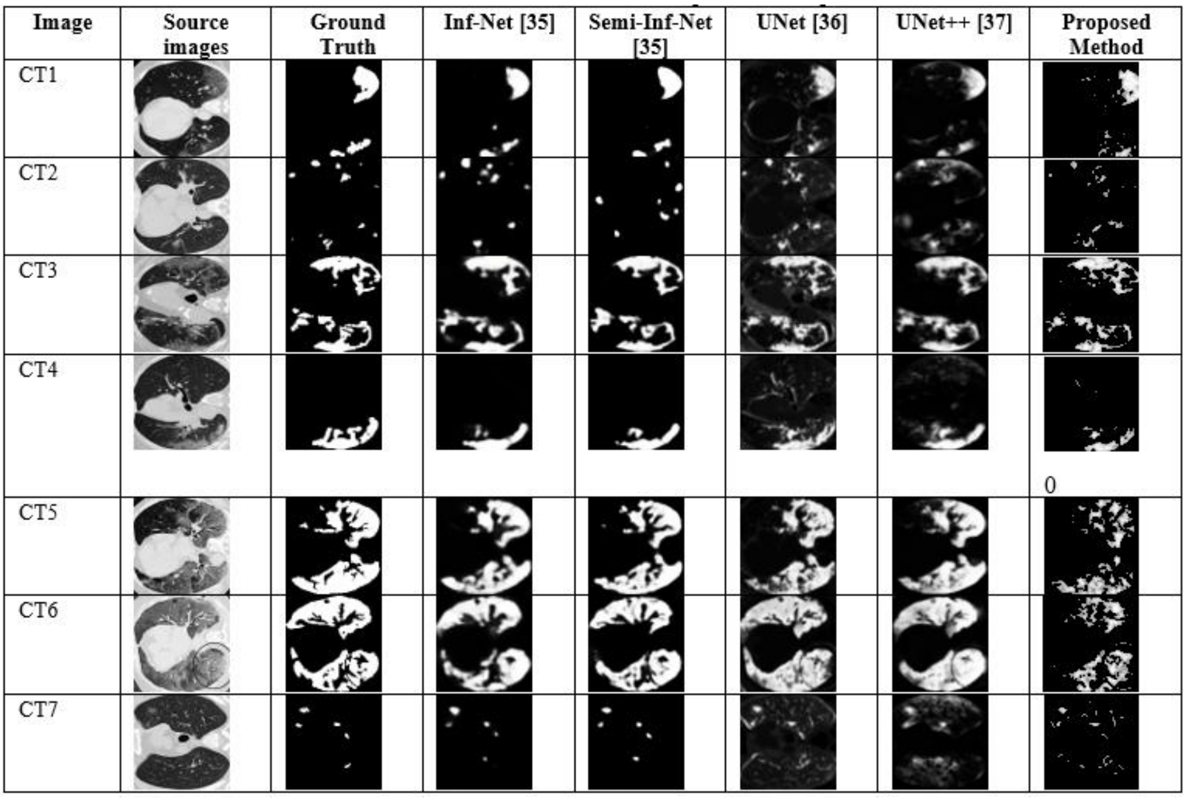

Figure 3. Visual comparison of the findings of the segmentation of lung infections

Table 1. Comparison of the proposed approach with other segmentation approaches using seven COVID-19 images

Images	Metrics	Inf-Net	Semi-Inf-Net	UNet	UNet++	Proposed Method
CT1	Time (s)	184	174	190	200	16.8803
	Accuracy	0.9719	0.9749	0.9502	0.9516	0.9809
	Sensitivity	0.7506	0.7664	0.6226	0.7385	0.7653
	Fmeasure	0.8294	0.8472	0.6945	0.7743	0.8503
	Precision	0.9265	0.9470	0.7851	0.8138	0.9574
	MCC	0.8196	0.8392	0.6731	0.7540	0.8484
	Dice	0.8294	0.8472	0.6945	0.7743	0.8503
	Jaccard	0.7085	0.7349	0.5319	0.6318	0.7398
	Specitivity	0.9941	0.9957	0.9830	0.9831	0.9944
CT2	Time (s)	190	170	210	205	21.7729
	Accuracy	0.9802	0.9873	0.9585	0.8906	0.9883
	Sensitivity	0.7666	0.6777	0.6405	0.5282	0.9073
	Fmeasure	0.6464	0.7149	0.4212	0.2810	0.7401
	Precision	0.5588	0.7565	0.3137	0.1663	0.7773
	MCC	0.6450	0.7095	0.4300	0.3614	0.7307
	Dice	0.6464	0.7149	0.4212	0.2810	0.7401
	Jaccard	0.4776	0.5563	0.2668	0.1635	0.5822
	Specitivity	0.9854	0.9947	0.9662	0.8902	0.9960
CT3	Time (s)	150	167	201	199	18.6662
	Accuracy	0.9215	0.9345	0.8745	0.9385	0.9497
	Sensitivity	0.8313	0.8598	0.6578	0.6964	0.9002
	Fmeasure	0.8100	0.8410	0.6785	0.7365	0.8549
	Precision	0.7897	0.8229	0.7006	0.7815	0.8140
	MCC	0.7609	0.8001	0.6011	0.8177	0.8765
	Dice	0.8100	0.8410	0.6785	0.8549	0.8465
	Jaccard	0.6806	0.7256	0.5135	0.7466	0.7829
	Specitivity	0.9442	0.9533	0.9291	0.9481	0.9549
CT4	Time (s)	188	193	220	217	24.4575
	Accuracy	0.9591	0.9611	0.9332	0.9599	0.9710
	Sensitivity	0.6542	0.6389	0.5840	0.6869	0.6423
	Fmeasure	0.7389	0.7439	0.6074	0.7517	0.7577
	Precision	0.8487	0.8900	0.6326	0.8301	0.8546
	MCC	0.7242	0.7351	0.5715	0.7340	0.7486
	Dice	0.7389	0.7439	0.6074	0.7517	0.7577
	Jaccard	0.5859	0.5922	0.4361	0.6022	0.6867
	Specitivity	0.9887	0.9923	0.9671	0.9864	0.9961
CT5	Time (s)	182	185	230	219	23.8499
	Accuracy	0.9251	0.9313	0.8874	0.9328	0.9347
	Sensitivity	0.8455	0.8432	0.7623	0.8793	0.8852
	Fmeasure	0.8785	0.8871	0.8125	0.8239	0.8960
	Precision	0.9141	0.9358	0.8698	0.9134	0.9537
	MCC	0.8258	0.8403	0.7358	0.8488	0.8518
	Dice	0.8785	0.8871	0.8125	0. 6239	0. 8960
	Jaccard	0.7833	0.7971	0.6842	0. 4534	0. 8116
	Specitivity	0.9626	0.9728	0.9463	0.9607	0.9770
CT6	Time (s)	191	184	207	218	23.9660
	Accuracy	0.8875	0.8944	0.8575	0.8845	0.8885
	Sensitivity	0.8203	0.8288	0.8924	0.4526	0.9179
	Fmeasure	0.8401	0.8497	0.8186	0.5912	0.8547
	Precision	0.8609	0.8718	0.7560	0.7996	0.8820
	MCC	0.7540	0.7690	0.7091	0.4983	0.7685
	Dice	0.8401	0.8497	0.8186	0.5912	0.8547
	Jaccard	0.7243	0.7387	0.6929	0.4196	0.7462
	Specitivity	0.9253	0.9314	0.8378	0.8704	0.9557
CT7	Time (s)	184	178	217	226	19.8066
	Accuracy	0.9913	0.9929	0.9482	0.8668	0.9959
	Sensitivity	0.6369	0.7200	0.8930	0.8521	0.8945
	Fmeasure	0.5995	0.6730	0.2600	0.1153	0.6383
	Precision	0.5663	0.6316	0.1522	0.0619	0.6349
	MCC	0.5962	0.6708	0.3565	0.2079	0.6771
	Dice	0.5995	0.6730	0.2600	0.1153	0.7383
	Jaccard	0.4281	0.5071	0.1494	0.0612	0.5036
	Specitivity	0.9950	0.9957	0.9488	0.8669	0.9977

Qualitative Results: The findings of the segmentation of the lung infection, which are illustrated in Figure 3, suggest that the proposed method works better than the methods used by the other researchers noticeably. In particular, they produce segmentation results which are near to the ground-truth and contain less mis-segmented tissue. U-Net and U-Net++, on the other hand, present dissatisfying results, with a significant number of improperly segmented tissues. Although the results are improved by using Inf-Net, this method is still unpromising. The method that we proposed was much more effective than the other methods. It was better able to identify the pixels of the white and gray parts areas more obviously. Consequently, this technique imitates the process that actual clinicians use to segment lung infection areas from CT slices; as a result, it achieves a performance that is quite promising.

We also provide the results of the CT images dataset [31] in Figure 4. As can be shown, the proposed hybrid technique constantly achieves the best results compared to all of the other techniques. The results of the experiments showed that the proposed technique was superior in terms of accurately obtaining lung infection segmentation from the original CT images.

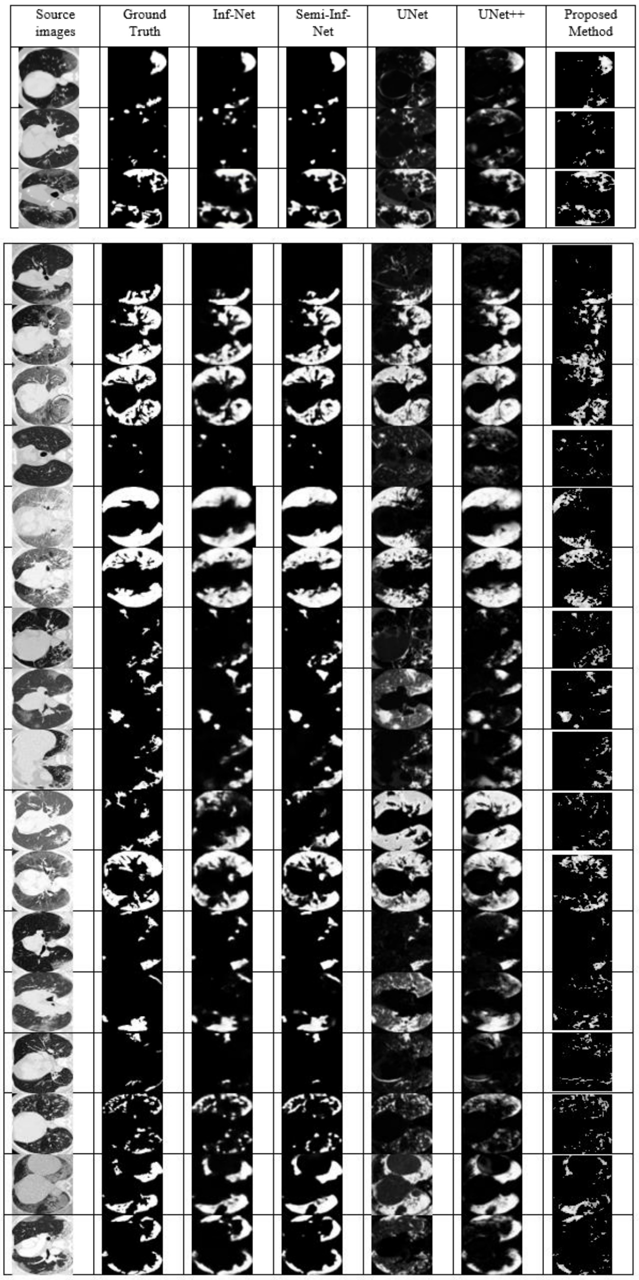

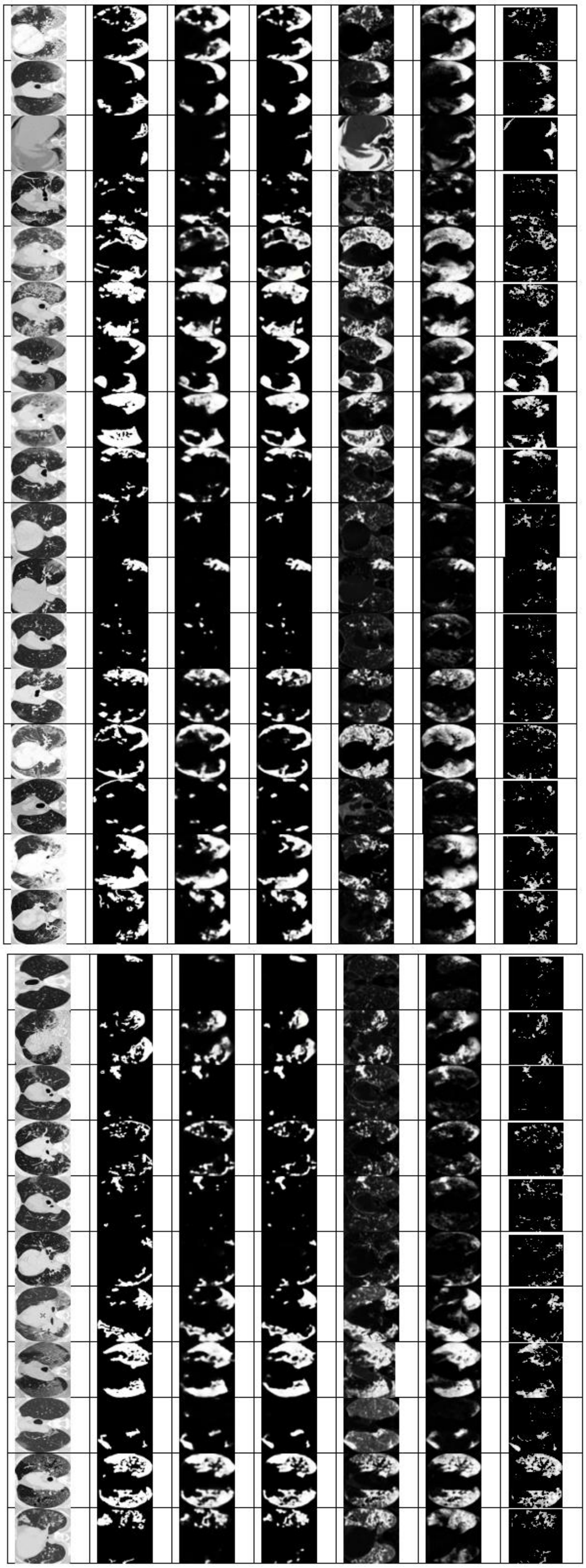

Figure 4. Visual comparison of the findings of the segmentation of lung infections of dataset

5. CONCLUSIONS

Researchers working in the field of computer vision face a significant obstacle in the form of an accurate segmentation of CT scan images. As a result, the purpose of this work was to offer a hybrid approach for segmenting images of lung CT infections taken from patients diagnosed with COVID-19. the method combining UWT, fuzzy C-means clustering, and ADF successfully yielded segmented images of a high quality. UWT based FCMC was utilized to get pixels of the white and gray matter more obviously. Over and above, the ADF was utilized to eliminate the intrinsic ambiguities, impreciseness, uncertainties, and noise from the resulting segmented images.

The proposed approach has considerable potential for use in analyzing COVID-19 diagnosis, such as quantifying infected areas and tracking longitudinal sickness change. It should be noted that the suggested approach can detect items with low intensity contrast between natural tissues and infections. This phenomenon frequently occurs in natural disguise objects.

Even though earlier research has demonstrated that deep learning models [35] had good segmentation performance, the hybrid method that was presented still managed to outperform the models that were currently in use on the small dataset. In the future, we plan to apply the proposed method to segment other kinds of CT images by changeful the segmentation processes.

REFERENCES

[1] Paules, C.I., Marston, H.D., Fauci, A.S. (2020). Coronavirus infections-more than just the common cold. Jama Network, 323(8): 707-708. https://doi.org/10.1001/jama.2020.0757

[2] World Health Organization. (2020). Naming the coronavirus disease (COVID-19) and the virus that causes it. Brazilian Journal of Implantology and Health Sciences, 2(3).

[3] Wu, Y.H., Gao, S.H., Mei, J., Xu, J., Fan, D.P., Zhang, R.G., Cheng, M.M. (2021). JCS: An explainable COVID-19 diagnosis system by joint classification and segmentation. In IEEE Transactions on Image Processing, IEEE, 30: 3113-3126. https://doi.org/10.1109/TIP.2021.3058783

[4] Chung, M., Bernheim, A., Mei, X.Y., Zhang, N., Huang, M.Q., Zeng, X.J., Cui, J.F., Xu, W.J., Yang, Y., Fayad, Z.A., Jacobi, A., Li, K.W., Li, S.L., Shan, H. (2020). CT imaging features of 2019 novel coronavirus (2019-nCoV). Radiology, 295(1): 202-207. https://doi.org/10.1148/radiol.2020200230

[5] Bernheim, A., Mei, X.Y., Huang, M.Q., Yang, Y., Fayad, Z.A., Zhang, N., Diao, K.Y., Lin, B., Zhu, X.Q., Li, K.W., Li, S.L., Shan, H., Jacobi, A., Chung, M. (2020). Chest CT findings in coronavirus disease-19 (COVID-19): relationship to duration of infection. Radiology, 295(3): 685-691. https://doi.org/10.1148/radiol.2020200463

[6] Shi, F., Wang, J., Shi, J., Wu, Z.Y., Wang, Q., Tang, Z.Y., He, K., Shi, Y.H., Shen, D.G. (2020). Review of artificial intelligence techniques in imaging data acquisition, segmentation, and diagnosis for COVID-19. In IEEE Reviews in Biomedical Engineering, IEEE, 14: 4-15. https://doi.org/10.1109/RBME.2020.2987975

[7] Xu, R., Wunsch, D. (2005). Survey of clustering algorithms. In IEEE Transactions on Neural Networks, IEEE, 16(3): 645-678.https://doi.org/10.1109/TNN.2005.845141

[8] Moftah, H.M., Azar, A.T., Al-Shammari, E.T., Ghali, N.I., Hassanien, A.E., Shoman, M. (2014). Adaptive k-means clustering algorithm for MR breast image segmentation. Neural Computing and Applications, 24: 1917-1928. https://doi.org/10.1007/s00521-013-1437-4

[9] Huang, Y.P., Singh, P., Kuo, H.C. (2020). A hybrid fuzzy clustering approach for the recognition and visualization of MRI images of Parkinson's disease. In IEEE Access, IEEE, 8: 25041-25051. https://doi.org/10.1109/ACCESS.2020.2969806

[10] Tinnathi, S., Sudhavani, G. (2021). An efficient copy move for gery detection using adaptive watershed segmentation with AGSO and hybrid feature extraction. Journal of Visual Communication and Image Representation, 74: 102966. https://doi.org/10.1016/j.jvcir.2020.102966

[11] Mallat, S.G. (1989). A theory for multiresolution signal decomposition: the wavelet representation. In IEEE Transactions on Pattern Analysis and Machine Intelligence, IEEE, 11(7): 674-693. https://doi.org/10.1109/34.192463

[12] Otsu, N. (1979). A threshold selection method from gray-level histograms. In IEEE Transactions on Systems, Man, and Cybernetics, IEEE, 9(1): 62-66. https://doi.org/10.1109/TSMC.1979.4310076

[13] Lifton, J., Liu, T. (2021). An adaptive thresholding algorithm for porosity measurement of additively manufactured metal test samples via X-ray computed tomography. Additive Manufacturing, 39: 101899. https://doi.org/10.1016/j.addma.2021.101899

[14] Deng, H., Fitts, J.P., Peters, C.A. (2016). Quantifying fracture geometry with X-ray tomography: Technique of iterative local thresholding (TILT) for 3D image segmentation. Computational Geosciences, 20: 231-244. https://doi.org/10.1007/s10596-016-9560-9

[15] Zhang, L.P. (2020). A medical image segmentation methods based on SOM and wavelet transforms. InMIPPR 2019: Automatic Target Recognition and Navigation, SPIE, 11429: 25-30. https://doi.org/10.1117/12.2535794

[16] Mohsen, H., El-Dahshan, E.S.A., El-Horbaty, E.S.M., Salem, A.B.M. (2018). Classification using deep learning neural networks for brain tumors. Future Computing and Informatics Journal, 3(1): 68-71. https://doi.org/10.1016/j.fcij.2017.12.001

[17] Jha, D., Riegler, M.A., Johansen, D.A., Halvorsen, P., Johansen, H.D. (2020). Doubleu-net: A deep convolutional neural network for medical image segmentation. In 2020 IEEE 33rd International Symposium on Computer-Based Medical Systems (CBMS), IEEE, pp. 558-564. https://doi.org/10.1109/CBMS49503.2020.00111

[18] Nason, G.P., Silverman, B.W. (1995). The stationary wavelet transform and some statistical applications. Wavelets and Statistics, 281-299. https://doi.org/10.1007/978-1-4612-2544-7_17

[19] Supratid, S., Aribarg, T., Supharatid, S. (2017). An integration of stationary wavelet transform and nonlinear autoregressive neural network with exogenous input for baseline and future forecasting of reservoir inflow. Water Resources Management, 31: 4023-4043. https://doi.org/10.1007/s11269-017-1726-2

[20] Naimi, H., Adamou-Mitiche, A.B.H., Mitiche, L. (2015). Medical image denoising using dual tree complex thresholding wavelet transform and Wiener filter. Journal of King Saud University-Computer and Information Sciences, 27(1): 40-45. https://doi.org/10.1016/j.jksuci.2014.03.015

[21] Naimi, H., Adamou-Mitiche, A., Mitiche, L. (2021). Lifting dual tree complex wavelets transform. International Journal of Electrical and Computer Engineering (IJECE), 11(5): 4008-4015. http://doi.org/10.11591/ijece.v11i5.pp4008-4015

[22] Juneau, P.M., Garnier, A., Duchesne, C. (2015). The undecimated wavelet transform–multivariate image analysis (UWT-MIA) for simultaneous extraction of spectral and spatial information. Chemometrics and Intelligent Laboratory Systems, 142: 304-318. https://doi.org/10.1016/j.chemolab.2014.09.007

[23] Naimi, H. (2022). Performance and quality assurance of medical image using hybrid thresholding wavelet transform with Wiener filter. Australian Journal of Electrical and Electronics Engineering, 19(3): 294-299. https://doi.org/10.1080/1448837X.2022.2034350

[24] Jiang, Q., Jin, X., Lee, S.J., Yao, S.W. (2017). A novel multi-focus image fusion method based on stationary wavelet transform and local features of fuzzy sets. In IEEE Access, IEEE, 5: 20286-20302. https://doi.org/10.1109/ACCESS.2017.2758644

[25] Naimi, H., Adamou-Mitiche, A.B.H., Mitiche, L. (2021). Hybrid thresholding lifting dual tree complex wavelet transform with wiener filter for quality assurance of medical image. In 2021 12th International Conference on Information and Communication Systems (ICICS), IEEE, pp. 228-233. https://doi.org/10.1109/ICICS52457.2021.9464625

[26] Dhanachandra, N., Chanu, Y.J. (2020). An image segmentation approach based on fuzzy c-means and dynamic particle swarm optimization algorithm. Multimedia Tools and Applications, 79(25-26): 18839-18858. https://doi.org/10.1007/s11042-020-08699-8

[27] Ganguly, S., Bose, D., Konar, A. (2013). Clustering using vector membership: an extension of the fuzzy c-means algorithm. In 2013 Fifth International Conference on Advanced Computing (ICoAC), IEEE, pp. 27-32. https://doi.org/10.1109/ICoAC.2013.6921922

[28] Cuevas, E., Becerra, H., Luque, A. (2021). Anisotropic diffusion filtering through multi-objective optimization. Mathematics and Computers in Simulation, 181: 410-429. https://doi.org/10.1016/j.matcom.2020.09.030

[29] Artyukov, I.A., Irtuganov, N.N. (2019). Noise-driven anisotropic diffusion filtering for X-Ray low contrast imaging. Journal of Russian Laser Research, 40: 150-154. https://doi.org/10.1007/s10946-019-09782-8

[30] Rossovskii, L.E. (2017). Image filtering with the use of anisotropic diffusion. Computational Mathematics and Mathematical Physics, 57: 401-408. https://doi.org/10.1134/S0965542517030125

[31] Jenssen, H.B. (2020). Covid-19 CT segmentation dataset. http://medicalsegmentation.com/covid19/, accessed on April 10, 2020.

[32] HosseiniPanah, S., Zamani, A., Emadi, F., HamtaeiPour, F. (2019). Multiple sclerosis lesions segmentation in magnetic resonance imaging using ensemble support vector machine (ESVM). Journal of Biomedical Physics & Engineering, 9(6): 699. https://doi.org/10.31661/jbpe.v0i0.986

[33] Chicco, D. (2017). Ten quick tips for machine learning in computational biology. BioData Mining, 10(1): 35. https://doi.org/10.1186/s13040-017-0155-3

[34] Chicco, D., Jurman, G. (2020). The advantages of the Matthews correlation coefficient (MCC) over F1 score and accuracy in binary classification evaluation. BMC Genomics, 21: 1-13. https://doi.org/10.1186/s12864-019-6413-7

[35] Fan, D.P., Zhou, T., Ji, G.P., Zhou, Y., Chen, G., Fu, H.Z., Shen, J.B., Shao, L. (2020). Inf-net: Automatic covid-19 lung infection segmentation from CT images. In IEEE Transactions on Medical Imaging, IEEE, 39(8): 2626-2637.https://doi.org/10.1109/TMI.2020.2996645

[36] Ronneberger, O., Fischer, P., Brox, T. (2015). U-net: Convolutional networks for biomedical image segmentation. In Medical Image Computing and Computer-Assisted Intervention-MICCAI 2015: 18th International Conference, Proceedings, Springer International Publishing, 18: 234-241. https://doi.org/10.1007/978-3-319-24574-4_28

[37] Zhou, Z.W., Rahman Siddiquee, M.M., Tajbakhsh, N., Liang, J.M. (2018). Unet++: A nested u-net architecture for medical image segmentation. In Deep Learning in Medical Image Analysis and Multimodal Learning for Clinical Decision Support: 4th International Workshop, DLMIA 2018, and 8th International Workshop, ML-CDS 2018, Held in Conjunction with MICCAI 2018, Proceedings, Springer International Publishing, 4: 3-11. https://doi.org/10.1007/978-3-030-00889-5_1

NOMENCLATURE

g_j^n, g_k^n	Low Pass Filters
h_j^n, h_k^n	High Pass Filters
x_n	the low frequency sub-band at levels n
x_{n+1}	the low frequency sub-band at levels n+1
x_{n+1}^h	the horizontal detail coefficients at level n+1
x_{n+1}^v	the vertical detail coefficients, at level n+1
x_{n+1}^d	the diagonal detail coefficients, at level n+1
$\tilde{g}_j^n, \tilde{g}_k^n$	the reconstruction of low pass filters
$\tilde{h}_j^n, \tilde{h}_k^n$	the reconstruction of high pass filters
$\tilde{x}_n$	the reconstruction low frequency sub-band at levels n
$\tilde{x}_{n+1}$	the reconstruction low frequency sub-band at levels n+1
$\tilde{x}_{n+1}^h$	the reconstructed horizontal, detail coefficients
$\tilde{x}_{n+1}^v$	the reconstructed vertical detail coefficients
$\tilde{x}_{n+1}^d$	the reconstructed diagonal detail coefficients
x_i	the i^{th} data point
v_j	the j^{th} cluster center
μ_{ij}	the degree of membership of the ith data point to the j^{th} cluster

Greek symbols

ω	the input wavelet coefficients
z	the output wavelet coefficients
σ	the noise level

λ	the selected Shrinkage value	c	the number of clusters
N	the signal's size	m	is a fuzziness parameter that determines the degree of fuzziness in the clustering.